



## Regular Article

## Oxidation behaviour of a next generation polycrystalline Mn containing Ni-based superalloy

S. Pedrazzini<sup>a,\*</sup>, D.J. Child<sup>b</sup>, G. West<sup>c</sup>, S.S. Doak<sup>c</sup>, M.C. Hardy<sup>b</sup>, M.P. Moody<sup>a</sup>, P.A.J. Bagot<sup>a</sup><sup>a</sup> Department of Materials, University of Oxford, Parks Road, OX1 3PH Oxford, UK<sup>b</sup> Rolls-Royce plc., Derby, UK<sup>c</sup> Department of Materials, Loughborough University, LE11 3TU Loughborough, UK

## ARTICLE INFO

## Article history:

Received 29 July 2015

Received in revised form 2 October 2015

Accepted 2 October 2015

Available online 23 October 2015

## Keywords:

Ni-based superalloy

Manganese

Atom Probe Tomography

Oxidation

## ABSTRACT

A prototype next-generation superalloy containing 1 at.% Mn was oxidised in air at 800 °C for 100 h, and compared with a commercial Ni-based superalloy. The oxide scale consisted of a multi-phase layered structure measured by Atom Probe Tomography as uppermost NiCr<sub>2</sub>Mn<sub>2</sub>O<sub>4</sub>, followed by an inhomogeneous mix of Cr<sub>2</sub>O<sub>3</sub>, spinel MnCr<sub>2</sub>O<sub>4</sub> and rutile (Ti,Cr)O<sub>2</sub>. The Mn did not form a homogeneous, surface passivating oxide layer. Despite this, the alloy showed a 3 × reduction of oxide thickness compared to a commercial polycrystalline Ni-based superalloy.

© 2015 Elsevier Ltd. All rights reserved.

Polycrystalline Ni-superalloys are used extensively in gas-turbine discs, where they are utilised at temperatures close to their melting point for timescales which extend to thousands of hours [1]. Thermally grown oxides, which form at such temperatures, can cause a degradation of the mechanical properties through both the removal of solutes from solid solution and dissolution of strengthening phases from the oxide-affected zone [2,3]. The oxide growth rate and extent of the oxide-affected zone, as well as high temperature tensile, fatigue and creep properties are all strongly dependent on the alloy chemistry. The superior oxidation resistance of some Ni-based superalloys results from the formation of a continuous Al<sub>2</sub>O<sub>3</sub> or Cr<sub>2</sub>O<sub>3</sub> film that creates a barrier, passivating the surface and preventing further oxidation [4]. However, in such complex multicomponent alloys minor alloying additions can also strongly influence oxidation, allowing considerable scope for composition optimisation. For example recent studies have focussed on the beneficial or detrimental effect additions of Ta, W, Nb and Ti have on oxidation [5–7]. Non-metallic species such as Si can also dramatically influence the oxidation kinetics. Si is known to promote the formation of a continuous layer of alumina by generating heterogeneous nucleation sites [4]. However, Si may also adversely affect the tensile and creep properties through grain boundary embrittlement and by triggering the formation acicular Topologically Close Packed (TCP) phases. These act as stress concentration sites, initiating fracture and causing premature failure [8]. Due to its tendency to cause undesirable phase formation at the grain boundaries Si can only be added to single crystal

superalloys (such as directionally solidified turbine blade alloys), but cannot be utilised for applications which require polycrystalline alloys (such as turbine discs processed through powder metallurgy routes) [9]. In a prior study performed by X-ray diffraction (XRD) and Scanning Electron Microscopy with Energy Dispersive X-ray spectroscopy (SEM-EDX) of a single crystal model Ni-20Cr alloy containing 1 wt.% Si, a further addition of 3 wt.% Mn was shown to produce a highly protective MnCr<sub>2</sub>O<sub>4</sub> spinel layer beneath the Cr<sub>2</sub>O<sub>3</sub> scale [10]. This spinel reduced the growth speed of the oxide scale by 1000 times when compared with the same Mn-free alloy. It also exhibited improved oxide-metal adhesion, reducing the risk of spallation. Si was shown by SEM-EDX to segregate to the spinel and was thought to promote its formation. The oxidation behaviour of a polycrystalline alloy containing Mn, in which Si cannot be utilised as a nucleation catalyst for MnCr<sub>2</sub>O<sub>4</sub> spinel, has never been analysed. High-resolution characterisation studies exploring the effects and potential benefits of Mn on the oxidation behaviour of new generation alloys have never been performed and are required to properly understand the oxide-metal microstructures formed.

Most characterisation studies of oxidised samples are performed using a combination of XRD and either SEM or Transmission Electron Microscopy (TEM) associated with EDX [11–13]. Atom Probe Tomography is a high-resolution characterisation technique, which provides unparalleled spatial and chemical resolution on the nanoscale giving invaluable insight in oxidation mechanisms [14]. Due to the inherent difficulty involved in obtaining datasets from brittle, thermally and electrically insulating samples, in-depth studies of oxidation behaviour which encompass 3D distributions of chemical compositions and segregation performed using Atom Probe Tomography (APT) have until

\* Corresponding author.

**Table 1**

Chemical composition of the V207J and RR1000 alloys used in the present study, as measured by ICP-OES analysis.

At.%	V207J	RR1000
Ni	Bal.	Bal.
Cr	16	16.5
Co	4	18
Fe	9	0
Si	0	0
<b>Mn</b>	<b>1</b>	<b>0</b>
Mo	1.35	3
W	0.9	0
Al	5.5	6.4
Nb	3.5	0
Ti	1	4.3
Ta	0.7	0.6
C	0.15	0.13
B	0.15	0.08
Zr	0.035	0.04

recently been limited [2,3]. However, recent developments both in instrumentation and sample preparation techniques are now facilitating measurements [15–19]. In the present study, a multi-scale investigation was performed using a suite of characterisation techniques to provide an understanding of the oxidation behaviour of a 1 at.% Mn prototype superalloy.

A 15 mm diameter, approximately 2 mm thick sample of a Ni superalloy named V207J [20] (containing 1 at.% Mn) produced using powder metallurgy was provided by Rolls-Royce plc. The button was ground and polished to 0.25  $\mu\text{m}$  grit size on all faces and edges were chamfered at 45° by 1 mm. The surface roughness ( $R_a$ ) was measured by a white light interferometer to be 209 nm. The button was then placed in a furnace stabilised at 800 °C for 100 h in air. A comparable fine grain (FG) (~5  $\mu\text{m}$  dia.) RR1000 alloy specimen was also exposed to the same thermal conditions. After 100 h at 800 °C both the FG RR1000 and the V207J samples had formed oxide layers. After exposure, specimens were air-cooled and mounted with silver epoxy on Al stubs for SEM. The chemical compositions of both alloys tested in the present study was measured using Inductively Coupled Plasma-Optical Emission Spectrometry (ICP-OES) analysis and is shown in Table 1.

A first overview of the morphology of the oxide was obtained through Focused Ion Beam (FIB) and SEM analysis. Micrographs were obtained using a Zeiss NVision dual beam microscope. Cross-sections were cut into the sample using the FIB. A representative FIB ion beam micrograph of the oxidised region of V207J alloy is shown in Fig. 1. The micrograph provides a first insight in the different phases present in the oxide-affected zone. The chromia and spinel surface scale is visible, along with a discontinuous layer directly underneath. The  $\gamma'$  denuded zone was found to be between 1–2  $\mu\text{m}$  in depth, and within it extensive regions of lath-like phases were observed. Some sub-surface

**Table 2**

Oxide thickness measurements obtained from over 50 individual regions identified in SEM micrographs. A 2.3 $\times$  reduction of oxide scale thickness in the V207J superalloy is noted when compared with commercial fine grained RR1000.

Alloy	Chromia /spinel scale	Alumina depth	Total
V207J	0.46 $\pm$ 0.17	0.53 $\pm$ 0.28	0.99
FG RR1000	1.05 $\pm$ 0.20	2.11 $\pm$ 0.44	3.16

grains were also visible within the denuded zone along with inter- and intra-granular  $\text{Al}_2\text{O}_3$  particles. Finally, small amounts of residual  $\gamma$  were also observed in the oxide scale. As an established alloy, the oxidation behaviour of FG RR1000 has been studied extensively, e.g. [21], showing a similar oxide scale layout to the V207J alloy after thermal ageing for 100 h at 800 °C in air. The oxide scale and  $\text{Al}_2\text{O}_3$  “finger” depth were measured from SEM micrographs and are shown in Table 2. Five measurements of oxidation damage depths per image were performed, using Image J software over 10 images. Values reported are mean  $\pm$  standard deviation. These measurements show an average reduction by 2.3 $\times$  of the oxide scale thickness and a 4 $\times$  reduction in alumina finger depth when comparing the V207J alloy with FG RR1000 oxidised under the same conditions. Several reasons could explain the reduction in oxide layer thickness, based on both the Mn content and other compositional differences between the V207J and RR1000 alloys studied, therefore further characterisation has been undertaken to elucidate their effects.

An accurate measure of the chemical composition variation with depth was obtained through XPS analysis (K-Alpha, Thermo Fisher Scientific). XPS spectra sampling the oxide layer were acquired from two regions: in the centre and near the edge respectively, of the cross-sectioned V207J sample. The ion beam etching for this was carried out using 3 kV  $\text{Ar}^+$  ions, with a 1.2 mm  $\times$  1.2 mm raster area. The sample was rotated at 1 rpm during etching. The sample was then irradiated with monochromatic Al K $\alpha$  x-rays using a 50  $\mu\text{m}$  spot. Snapshot/scan data was acquired with 150/50 eV pass energies respectively. Fig. 2a shows an overview composition of the top 5  $\mu\text{m}$ , while Fig. 2b shows an enlargement of the uppermost 1  $\mu\text{m}$ . The XPS oxygen profile in Fig. 2a shows that while the oxide scale is 600 nm thick (in agreement with cross-sectional measurements) there is a shallow, decreasing oxygen gradient over ~3.5  $\mu\text{m}$ , after which the composition of the  $\gamma$  phase is reached. This gradient is a result of the intra- and inter-granular  $\text{Al}_2\text{O}_3$  extending inside the denuded zone. The initial Ni peak around 50 nm in depth in Fig. 2a is an indicator that Ni–Cr–Mn enriched spinels are likely forming. Mn enrichment is visible at the surface (top 550 nm), which could be an indicator of the presence of  $\text{MnCr}_2\text{O}_4$  spinel likely forming, as observed by other investigators [10]. The Ti enrichment is most likely an indicator of rutile formation in the top 400 nm, but could also be Ti in solid solution, as noted in chromia layer or various spinels in RR1000 [13]. However it is important to recall that

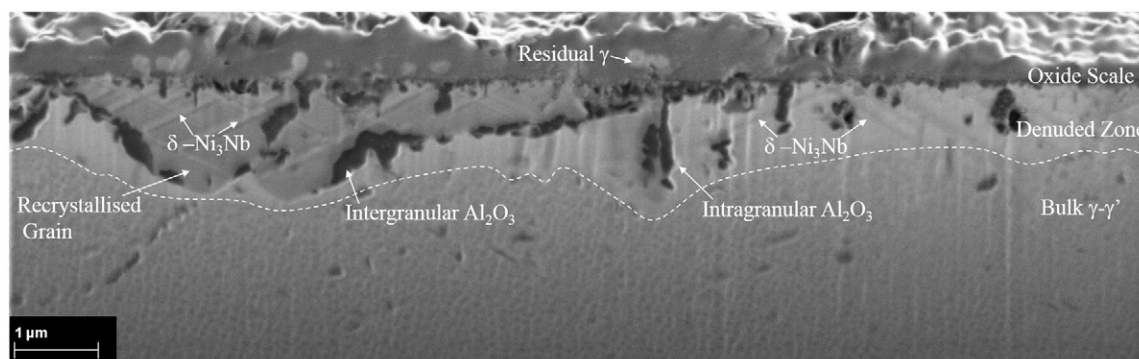


**Fig. 1.** FIB ion beam micrograph showing the features and phases present in the oxide-affected zone.

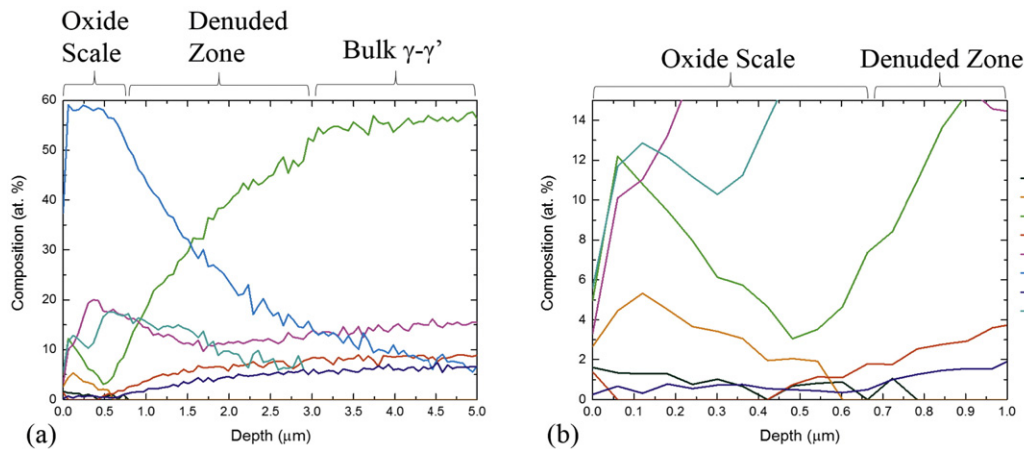


Fig. 2. (a) Overview of the chemical composition variations with depth and (b) enlargement of the surface oxide for improved resolution.

measurements by XPS are spatially restricted to within ‘craters’ ~1.2 mm in diameter, thus they provide an overall idea of the depth-dependent composition variations but not of localised segregation effects nor of different phases.

Atom Probe Tomography (APT) was therefore carried out on the samples to accurately identify such localised regions within the oxide scale. Samples for APT were prepared using a Zeiss NVision FIB. A tungsten protective capping layer was applied before extracting a cantilever sample ( $25 \times 5 \mu\text{m}$ ), which was mounted onto standard CAMECA Si microtip coupons. Mounted samples were then sharpened into tips  $<100 \text{ nm}$  in diameter. Low levels of porosity were observed in the oxide layer during FIB preparation of the APT samples. Samples were analysed using a CAMECA LEAP 3000X HR instrument at 200 kHz pulse rate, 0.4 nJ pulse energy and a stage temperature of 50 K. Datasets were collected and reconstructed using the standard CAMECA IVAS 3.6.6 software. Careful attention was paid to compositional accuracy when interpreting the resulting mass-to-charge-state spectra. A peak deconvolution algorithm was implemented where necessary to resolve peak overlaps in the spectrum, notably  $\text{Al}^+$  and  $\text{Cr}^{2+}$  at 27 Da. This peak deconvolution approach uses the natural isotopic abundance of each element to estimate the various contributions of the relative species to the overlapping peaks. An APT reconstruction is shown in Fig. 3a. The oxide scale is present, as well as the metal-oxide interface and the sub-oxide  $\gamma$  phase containing a  $\delta\text{-Ni}_3\text{Nb}$  intermetallic. Mn was found to partition to the upper surface spinel, whose composition was measured to be  $\text{NiCr}_2\text{Mn}_2\text{O}_4$ . It also partitions to the  $\text{Cr}_2\text{O}_3$  layer, creating a spinel incorporating regions of  $\text{Cr}_2\text{O}_3$  and  $\text{MnCr}_2\text{O}_4$ . No Mn was observed in the rutile phase, the sub-oxide bulk metallic  $\gamma$  or the  $\delta$  intermetallic phases. Phase separation can be observed within the oxide

scale itself. Beneath the uppermost  $\text{NiMn}_2\text{Cr}_2\text{O}_4$  section, alternating regions of  $\text{MnCr}_2\text{O}_4$  spinel and  $\text{Cr}_2\text{O}_3$  are observed. Interfaces have been demarcated for visual clarity in Fig. 3a using 25 at.% Cr, 3 at.% Mn, 5 at.% Ti and 5 at.% Nb iso-concentration surfaces. A region of rutile  $(\text{Ti,Cr})\text{O}_2$  is also apparent at the oxide-metal interface. The measured chemical compositions of the various oxidised regions are shown in Table 3. A 1D concentration profile across the  $\gamma$  –  $\text{MnCr}_2\text{O}_4$  metal-oxide interface, as indicated by the rectangular region of interest in Fig. 3a, is shown in Fig. 3b. It shows that Cr, Mn and small amounts of Ni partition to the oxide scale. The metal-oxide interface is sharp and no O enrichment is detected within the bulk metallic layer. The 1D concentration profile also goes through a section of a  $\delta\text{-Ni}_3\text{Nb}$  particle, which is visible beneath the oxide scale.

The main elements which affect oxidation behaviour of Ni-based superalloys are Ni, Cr and Al. Pettit et al. [22,1] through systematic studies using Ni–Al–Cr ternary alloys, created a classification dividing superalloys into three main sub-groups depending on the oxide layer they form. Both V207J and RR1000 belong to Group II: based on their nominal chemical composition, initially a transient oxide scale composed of  $\text{NiO}/\text{Ni}(\text{Al,Cr})_2\text{O}_4$  is predicted to form, followed by a sub-scale of  $\text{Cr}_2\text{O}_3$  and internal precipitation of  $\text{Al}_2\text{O}_3$ . This means that based on an Ellingham diagram, the expected oxide found on an equivalent alloy which is Mn free would be a layered structure containing a combination of the following stable oxides:  $\text{NiO}$ ,  $\text{Cr}_2\text{O}_3$  and finally  $\text{Al}_2\text{O}_3$ . The addition of Mn would be expected thermodynamically to encourage the formation of  $\text{MnO}$  or some spinels thereof. No data was found in the open scientific literature (or in any Thermocalc database available) containing the energy or oxygen partial pressure required for the formation of the spinels and oxidised phases observed in the present study, making

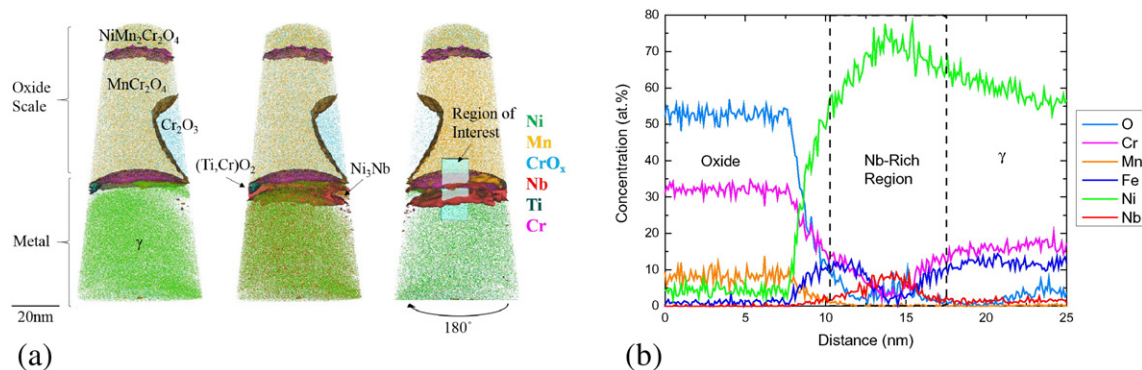


Fig. 3. (a) Atom maps showing the different types of oxides, spinels and the  $\delta$  phase in the denuded zone. In the third atom map a cuboidal volume was selected using the IVAS software “Region Of Interest” tool and (b) a 1D concentration profile was plotted across it going through the  $\delta$ -phase and into the  $\gamma$ .

**Table 3**

Composition (at.%) of each phase highlighted in Fig. 3, obtained by APT.

At.%	NiMn <sub>2</sub> Cr <sub>2</sub> O <sub>4</sub>	Cr <sub>2</sub> O <sub>3</sub>	MnCr <sub>2</sub> O <sub>4</sub>	Ni <sub>3</sub> Nb	(Ti,Cr)O <sub>2</sub>	γ
O	Bal.	Bal.	Bal.	–	Bal.	–
Mn	17.7	–	9.0	–	–	–
Cr	14.7	41.7	31.9	4.6	11.3	15.0
Ni	10.0	–	3.8	Bal.	8.4	Bal.
Ti	3.9	–	–	–	19.0	–
Co	–	–	1.3	4.7	–	6.0
Fe	5.2	–	–	5.6	1.4	13.1
Mo	–	–	–	2.1	–	1.4
W	–	–	–	1.3	–	1.0
Nb	–	–	–	11.1	–	1.3
Ta	–	–	–	–	7.0	–

thermodynamic predictions impractical at present. However, other differences in compositions between the V207J alloy and FG RR1000 could also be influencing oxidation resistance. V207J only contains 1 at.% Ti, compared to RR1000 which contains 4.3 at.% Ti. Ti is known to influence oxidation kinetics affecting the outcome of oxidation experiments. Most systematic studies on Ti alloying additions on oxidation behaviour of Ni based superalloys agree that the effect is generally deleterious, creating a substantial thickening of the oxide layer [11]. V207J also contains 3.5 at.% Nb, while RR1000 is Nb free. Nb is a known oxide former, though in the present alloy only sub-oxide formation of  $\delta$ -Ni<sub>3</sub>Nb phases was observed instead of Nb<sub>2</sub>O<sub>5</sub>.

The substantial reduction in oxide layer thickness when compared to a Mn free alloy is consistent with the results observed by Douglass and Armijo [10]. However, in contrast to the single MnCr<sub>2</sub>O<sub>4</sub> homogeneous passivating layer as previously concluded via lower resolution SEM-EDX and XRD analyses in that study [10], the current results demonstrate that a number of distinct nanometre-sized oxide phases and spinels have formed. This constitutes the first observation of such phases using a high-resolution analytical technique, and suggests that the combined effect of Cr<sub>2</sub>O<sub>3</sub> and MnCr<sub>2</sub>O<sub>4</sub> is sufficient to improve oxidation resistance.

## Acknowledgements

PAJB acknowledges a Royal Academy of Engineering Secondment to Rolls-Royce plc. The Oxford Atom Probe facility was funded by the EPSRC grant EP/D077664/1.

## References

- [1] R.C. Reed, *The Superalloys: Fundamentals and Applications*, Cambridge University Press, Cambridge, UK, 2012.
- [2] S.I. Baik, X. Yin, D.N. Seidman, *Scr. Mater.* 68 (11) (2013) 909–912.
- [3] Y. Chen, R.C. Reed, E.A. Marquis, *Scr. Mater.* 67 (9) (2012) 779–782.
- [4] M. Bensch, A. Sato, N. Warnken, E. Affeldt, R.C. Reed, U. Glatzel, *Acta Mater.* 60 (2012) 5468–5480.
- [5] L. Zheng, M. Zhang, J. Dong, *Appl. Surf. Sci.* 256 (2010) 7510–7515.
- [6] C. Rae, *Mater. Sci. Technol.* 25 (2009) 479–487.
- [7] Y. Amouyal, D.N. Seidman, *Acta Mater.* 59 (2011) 3321–3333.
- [8] A.C. Yeh, K. Kawagishi, H. Harada, T. Yokokawa, Y. Koizumi, T. Kobayashi, D.H. Ping, J. Fujioka, T. Suzuki, *Superalloy TMS Conference Proceedings 2008*, pp. 677–685.
- [9] M. Segersäll, P. Kontis, S. Pedrazzini, P.A.J. Bagot, M.P. Moody, J.J. Moverare, R.C. Reed, *Acta Mater.* 95 (2015) 456–467.
- [10] D.L. Douglass, J.S. Armijo, *Oxid. Met.* 2 (2) (1970) 207–231.
- [11] H. Nagai, M. Okabayashi, *Trans. Jpn. Inst. Mater.* 22 (10) (1981) 691–698.
- [12] M.A. Khan, S. Sundarajan, S. Natarajan, P. Parameswaran, E. Mohandas, *Mater. Manuf. Processes* 29 (2014) 832–839.
- [13] S. Cruchley, H.E. Evans, M.P. Taylor, M.C. Hardy, *Corros. Sci.* 75 (2013) 58–66.
- [14] T. Li, P.A.J. Bagot, E.A. Marquis, S.C. Edman Tsang, G.D.W. Smith, *Ultramic* 132 (2013) 205–211.
- [15] L. Viskari, M. Hornqvist, K.L. Moore, Y. Cao, K. Stiller, *Acta Mater.* 61 (10) (2013) 3630–3639.
- [16] H. Kitaguchi, M.P. Moody, H.Y. Li, H.E. Evans, M.C. Hardy, S. Lozano-Perez, *Scripta Mater.* 97 (2015) 41–44.
- [17] A. La Fontaine, H.-W. Yen, P.J. Felfer, S.P. Ringer, J.M. Cairney, *Scr. Mater.* 99 (2015) 1–4.
- [18] D.J. Young, T. Dinh Nguyen, P.J. Felfer, J. Zhang, J.M. Cairney, *Scr. Mater.* 77 (2014) 29–32.
- [19] A. La Fontaine, B. Gault, A. Breen, L. Stephenson, A. V. Ceguerra, L. Yang, T. Dinh Nguyen, J. Zhang, D. J. Young, J. M. Cairney, *Ultramicroscopy*, 2015, <http://dx.doi.org/10.1016/j.ultramic.2015.02.005>.
- [20] M.C. Hardy, European Patent Specification EP 2562277 B1, published 14.05.2014.
- [21] M.P. Taylor, H.E. Evans, S. Stekovic, M.C. Hardy, *Mater. High Temp.* 29 (2) (2012) 145–150.
- [22] F.S. Pettit, *Trans. AIME* 239 (1967) 1297–1305.